A STUDY ON CRACK PROPAGATION IN HETEROGENEOUS ELASTIC-PLASTIC SOLIDS

Kartik Srinivasan[1], Thomas Siegmund[1], Otmar Kolednik[2]

[1]School of Mechanical Engineering
Purdue University, West Lafayette, IN 47907, U.S.A.
ksriniv@ecn.purdue.edu
siegmund@ecn.purdue.edu

[2]Erich Schmid Institute of Materials Science
Austrian Academy of Science, A-8700 Leoben, Austria
kolednik@unileoben.ac.at

Abstract

In the vast majority of studies on ductile crack growth, the commonly made assumption is that of constant material properties along the crack path. Even in macroscopically homogeneous materials, however, the local material properties vary due to the random variation of the microstructure, e.g., variations in size, shape, and distribution of precipitates and inclusions. As a consequence, the crack propagation processes in ductile materials should be in a more realistic picture characterized by random fields of elastic-plastic material properties as well as random fields of the local parameters characterizing the material separation process. We report the results from 2D crack growth simulations in an elastic-plastic material conducted with the use of a cohesive zone model. The local randomness in the material parameters is accounted for through variations of the separation energy.

Introduction

For micro-ductile fracture, the separation energy, Γ, represents the plastic work per unit area required for the formation of the dimple structures on the two fracture surfaces. Stüwe [1], introduced a model to estimate the specific plastic strain energy to form the two dimpled fracture surfaces of a micro-ductile crack based on a model of void growth, R_{surf}. The result is

$$R_{surf} = S\bar{\sigma}(2h_0) \tag{1}$$

where $\bar{\sigma}$ is an appropriate mean flow stress of the material, which can be estimated by

$$\bar{\sigma} = \sigma_u \frac{exp(n)}{(1+n)n^n} . \tag{2}$$

σ_u is the ultimate tensile strength and n the (average) strain hardening coefficient, S denotes a shape factor of the dimples which has been found to be approximately $S \approx 0.25$ (Stüwe, [2]). In Eq. 1, h_0 is the dimple height. This value can be determined from the topography of the corresponding fracture surface regions on both specimen halves. The topographic measurements providing the basis for the present paper were performed by stereophoto-grammetric measurements using stereo image pairs taken in the scanning electron microscope by tilting the specimen. Such estimates have been introduced in Kolednik and Stüwe [3]. More modern stereophotogrammetric measurements, applying a digital image analysis system (Stampfl et al., [4]; Scherer and Kolednik, [5]), have been reported in Stampfl et al. [6], Stampfl and Kolednik [7] and Miserez et al. [8].

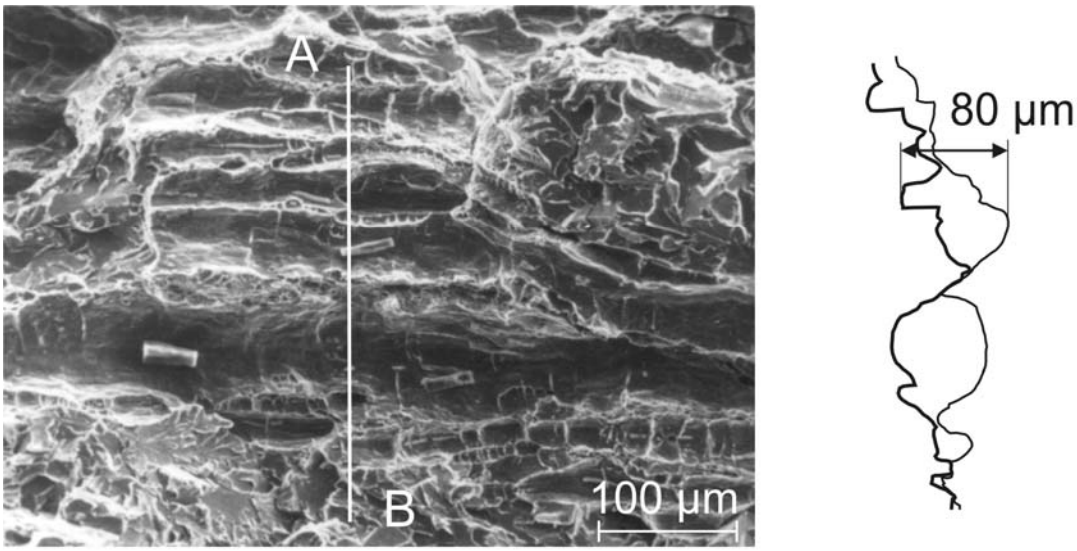

(a) (b)

FIGURE 1: (a) Fracture surface region of the steel St37 with narrow and broad dimples. Different broken pieces of MnS-inclusions are visible. (b) A crack profile. The thick line represents the fracture surface profile AB, the thin line the corresponding profile on the second specimen half.

A typical view of the fracture surface of the material under consideration, St37, is shown in Figure 1(a). As R_{surf} depends on the total dimple height, given by misfit between the two fracture surfaces, it is necessary to analyze corresponding regions on both halves of a broken specimen. Combining the information from two surfaces, a crack profile is obtained, Figure 1(b). From this diagram, a characteristic misfit of $2h_0 \approx 80$ µm is measured. This, inserted into Eq. 1 for $\bar{\sigma} \approx 600$ MPa, leads to a value of $R_{surf} \approx 12$ kJ/m^2. In this material, the dimple structure is mainly influenced by the distribution of the MnS inclusions. Due to the microstructural scatter, the dimple heights vary. Regions where small and large dimples occur together are observed in addition to regions with sequences of only smaller dimples. The latter regions can be up to a few hundreds of micrometers long. It should also be noted that crack extension is, considered at the microscopic scale, a discontinuous process of local blunting and extension steps (Turner and Kolednik, [9]). Accounting for this variation in dimple height, the value of R_{surf} is roughly estimated to be $R_{surf} \approx 12 \pm 4$ kJ/m^2. Adding a reasonable estimate for the specific energy for void initiation ($R_{vi} \approx 2$ kJ/m^2) to R_{surf}, we arrive at estimates for the separation energy, Γ. We obtain a mean value of $R_{surf} + R_{vi} \approx 14$ kJ/m^2 and corresponding minimal and maximum values of 10 kJ/m^2 and 18 kJ/m^2, respectively. The observed spatial variation of the separation energy motivates the simulation described in the present paper.

Material

The material investigated is an annealed mild steel with the German designation St37. The microstructure has ferrite grains with a mean intercept length of 17 µm with small carbide particles embedded and a distribution of MnS inclusions. In this paper, the bulk material properties are taken as Young's modulus $E = 200$ GPa, Poisson's ratio $\nu = 0.3$, yield strength $\sigma_y = 270$ MPa, ultimate tensile strength $\sigma_u = 426$ MPa, average strain hardening coefficient $n = 0.2$; Yan et al. [10]. Experimental results on multi-specimen fracture mechanics tests (CT-specimens of thickness $B = 25$ mm, width $W = 50$ mm, initial crack length $a_0 \approx 27$ mm)

were reported in Chen et al. [11]. The tests gave a valid J_{IC} = 120 kJ/m^2; the physical crack extension in the center region begins much earlier, J_i = 39 kJ/m^2 (Shan et al., [12]). No shear lips are seen on the fracture surfaces.

Cohesive zone modeling and data analysis

Mesh for the finite element modeling

The simulation of crack growth is performed by using the finite element code ABAQUS [13]. Half of the CT-specimen is modeled. 4-node plane strain elements are used for the bulk elements.

Cohesive elements are placed at the crack plane. Each cohesive element has two faces with 2 nodes on each face. The cohesive element has 2 integration points. The top face is connected with the adjacent bulk element, while the bottom face is connected with the y = 0 plane. Due to symmetry, only half models are analyzed. The size of the cohesive elements in the crack growth direction is 25 μm.

When no load is applied, the top face of the cohesive zone element coincides with the bottom face; when a tensile load is applied, the deformation of the bulk elements pulls the top face away from the bottom face. The constraint conditions are defined as following: u_y = 0 for the nodes at the plane y = 0 from the position of the last cohesive element in the x direction to the right-hand edge of the model; u_y = 0 for the nodes at the bottom faces of the cohesive elements; u_x = 0 for the nodes at the the point were the load is applied. The displacement is applied to the node at the left-hand edge of the model at position y = 19.5 mm. The load line displacement, v_{LL}, is obtained from the node at the left-hand edge of the model at the position y = 6.85 mm. Details of the model can be found in Chen et. al. [11].

The traction-separation behavior

Needleman's [14] traction–separation function is used to define the relationship between the cohesive normal traction, T, and the separation distance normal to the crack plane, δ, as follows:

$$T = \begin{cases} \dfrac{27}{4} T_{\max} \left(\dfrac{\delta}{\delta_f} \right) \left[1 - 2 \left(\dfrac{\delta}{\delta_f} \right) + \left(\dfrac{\delta}{\delta_f} \right)^2 \right] & \text{for } \delta \le \delta_f \\ 0 & \text{for } \delta > \delta_f \end{cases} \tag{3}$$

where $T_{\max}$ is the cohesive strength and δ_f the cohesive length. As a CT specimen geometry with only pure Mode I loading is considered, and as no shear lips appear at the side-surfaces of the St37 specimens, it is reasonable to consider only the normal separation. The normal separation energy, Γ, is defined as

$$\Gamma = \int_0^{\delta_f} T \, \mathrm{d}\delta \ . \tag{4}$$

Inserting Eq. 3 into Eq. 4, the relationship between the three parameters, Γ, $T_{\max}$, and δ_f is obtained as

$$\Gamma = \frac{9}{16} T_{\max} \delta_f \ . \tag{5}$$

In the model analyzed here a spatial variation of the separation energy was accounted for, while the value of the cohesive strength was kept constant. Based on the results described in Chen et al. [11], a plane strain calculation with Γ_{avg} = 16.0 kJ/m^2 and T_{max}= 1025 MPa can best fit the experimental data. Then, the observed scatter of ±20% variations in Γ were accounted by defining Γ_{min} = 12.8 kJ/m^2 for the first 250 μm, Γ_{max} = 19.2 kJ/m^2 for the next 250 μm, and so on. Figure 2 shows the traction–separation function, Eq. 3, for $\Gamma_{avg}, \Gamma_{min}, \Gamma_{max}$ used in the calculations.

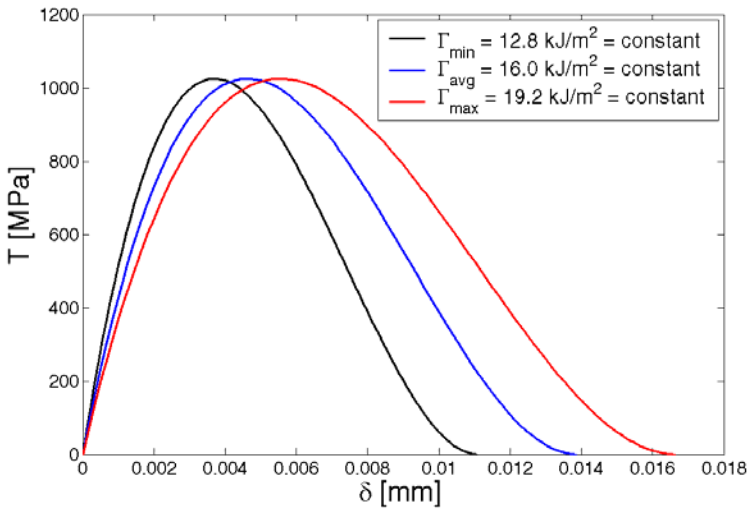

FIGURE 2. The traction separation relationship, Equation 3, for $\Gamma_{avg}, \Gamma_{min}, \Gamma_{max}$.

The crack tip is defined as the location with the largest value of x-coordinate connected to the initial crack at which the separation distance just reaches δ_f i.e. the tractions vanish. This is reasonable for micro-ductile fracture where the decreasing part of the traction–separation function shall reflect the weakening of the material in the process zone in front of the crack tip due to void growth and coalescence. Furthermore, we define a critical crack tip opening angle as the angle between the cohesive element faces at the instance of crack advance. This definition of *CTOA* is different from that used in many other studies, but useful for an understanding of the material separation process.

Results

Crack growth simulations were conducted for three sets of constant cohesive zone parameters prescribed in front of the crack tip, Γ_{avg}, Γ_{min}, Γ_{max} as well as for the case with spatially varying separation energy, $\Gamma=\Gamma(x)$. Figure 3 depicts the predicted data for the force F vs. the load line displacement, v_{LL}. Predicted data fall within the scatter band of the experimental data. For the computations with constant values of Γ, the cases Γ_{max} and Γ_{min} are above and below the prediction with Γ_{avg}. For the computation with $\Gamma=\Gamma(x)$, the computations predict an oscillating result. It should be noted that the prediction for the case $\Gamma=\Gamma(x)$ is below that of Γ_{avg}, despite the fact that the average separation energy for $\Gamma=\Gamma(x)$ is identical to Γ_{avg}. Instead, predictions for the case with spatially varying separation energy are close to those for Γ_{min}.

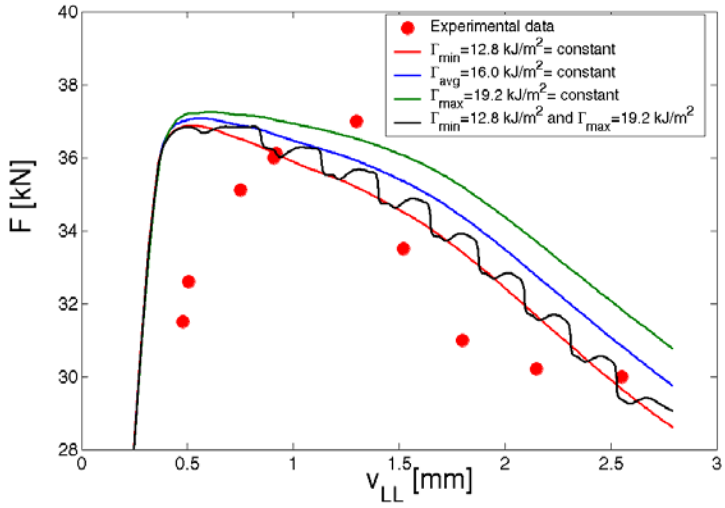

FIGURE 3: Predicted results for force vs. load line displacement. Comparison of cases with constant Γ to those with spatial variation in Γ.

The influence of the spatial variation in the separation energy is more clearly seen in the plot of crack extension, Δa , vs. load line displacement, v_{LL}, Figure 4(a). Again, the computational results compare well with experimental crack extension data measured at the midsection of the specimen. Predicted data for the case with spatially varying Γ show larger amounts of crack extension than for the case of Γ_{avg}. Crack extension rates show considerable local variation. As the crack propagates through a region with Γ_{min} the crack growth rate is large, however, at the transition to the area with Γ_{max}, significant crack retardation or even temporary crack arrest occurs before the crack continues to grow again. At the transition back to Γ_{min}, the crack growth rate is temporarily large such that at this point the crack essentially jumps ahead a distance of up to 100 μm. This crack jump is enabled by the formation of a secondary crack. Such a crack forms in front of the main crack when its tip approaches the area with Γ_{min}. In Figure 4(a), the secondary cracks are denoted by diamond-shaped symbols.

A further understanding of the crack propagation process under consideration of the secondary cracks is obtained by considering the crack tip opening angle at failure, $\delta = \delta_f$, in dependence of the position of a material element relative to the original crack tip. These results are depicted in Figure 4(b). From the results of many previous studies using the *CTOA* concept to study crack growth, one would expect an initially large value of *CTOA* that would reduce to a rather constant, smaller value as the crack propagates. Such a response is, however, present only on a "large" scale if spatial variations in the separation energy are accounted for. As the crack propagates through the initial 250 μm, an initially large value of *CTOA* is found, with a subsequent rapid decay. This decay in *CTOA* is stopped as the crack approaches the Γ_{max} area. Crack arrest then occurs and the value of *CTOA* increases significantly again for material elements still in the Γ_{min} area. Once the crack has overcome the arrest phase in Γ_{max}, *CTOA* decreases as the crack starts to grow again. It is important to observe, however, that *CTOA* at the later stages of growth in the Γ_{max} area drops rapidly and no steady state is reached. This drop in *CTOA* is due to the presence of the secondary crack that has now formed in front of the main crack. As the two cracks merge, the *CTOA* is reduced. This low value in *CTOA* is understood when considering the ratio between the remaining ligament between the main crack and the secondary crack to the cohesive length. If the ratio between these two dimensions becomes small, a transition from a crack type behaviour to a uniform debonding case occurs, Li et al. [15]. This stage of reduced *CTOA*

affects both the area of Γ_{max} as well as the subsequent Γ_{min}. After the main crack and the secondary crack have merged, with the tip now in the Γ_{min} area, *CTOA* tends to show again a crack growth type transition from a large *CTOA* to a small *CTOA* value. The drop in *CTOA* is, however, quickly stopped as the crack is arrested at the next transition to Γ_{max}. Subsequently, the process described repeats itself.

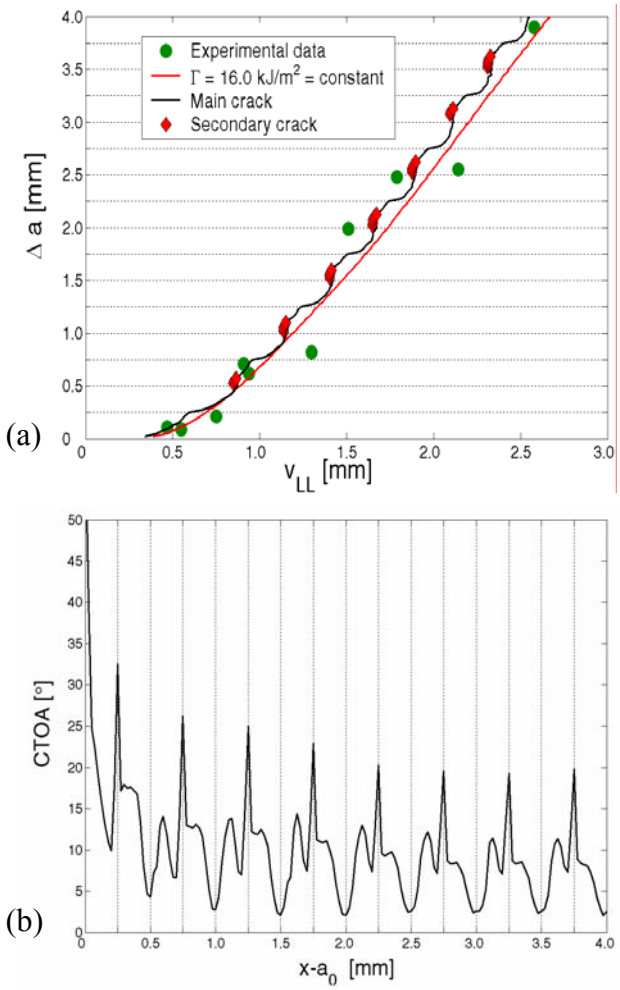

FIGURE 4: (a) Crack extension, Δa, vs. load line displacement, v_{LL} (b) The crack tip opening angle at the instance of failure ($\delta = \delta_f$) in dependence of the initial location in front of the original crack tip. Gridlines show the border between areas with Γ_{min} and Γ_{max}.

It is well known from previous studies of systems with major and minor cracks, e.g. in multi-site damaged thin sheet specimens, Li et al. [15], that the interaction between the major and minor cracks can significantly affect crack growth resistance. Here, crack growth resistance is quantified both by the use of the *J*-integral as well through the dissipation rate. The computed values for the *J*-integral are given for the cases Γ_{avg}, Γ_{min}, Γ_{max} as well as for $\Gamma = \Gamma(x)$ in Figure 5(a). The crack growth resistance predicted for the case with $\Gamma = \Gamma(x)$ is well below that of Γ_{avg}, and tends towards the values of *J* predicted for Γ_{min} as the amount of crack extension increases.

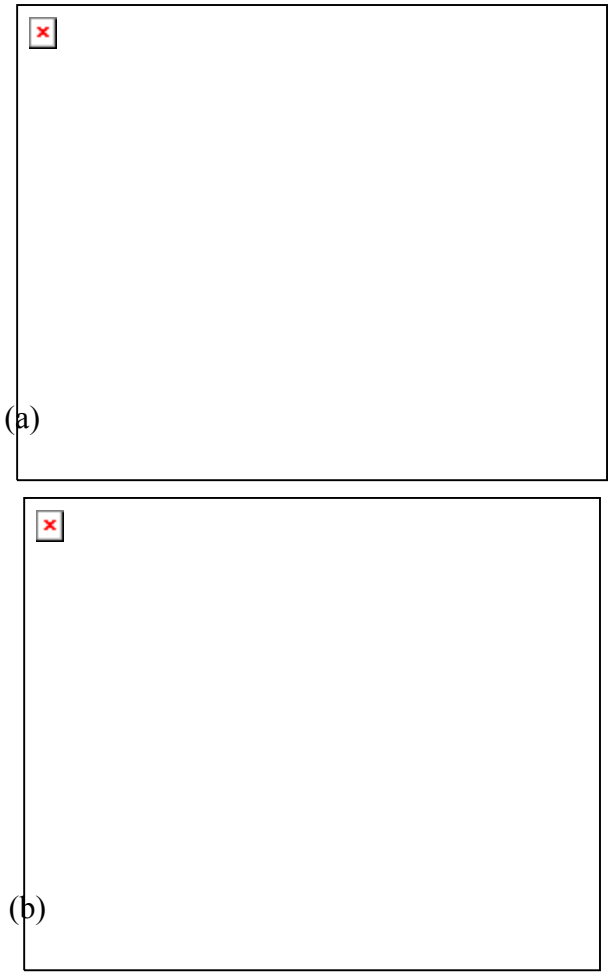

FIGURE 5: (a) Predicted values of *J*-integral in dependence of the crack extension, Δa . (b) Normalized dissipation rate, $R/\Gamma(x)$, vs. crack extension, Δa . Gridlines show the border between areas with Γ_{min} and Γ_{max}.

An even stronger deviation from the "average" behaviour is found if the dissipation rate is evaluated, Figure 5(b). Strong spikes in the dissipation rate occur during the crack arrest stage. The normalized value of the dissipation rate at that instance, $R/\Gamma(x)$, reaches values comparable to those found at the initiation of crack growth at the initial crack tip, thus by far exceeding the values of R/Γ found in calculations with constant values of the separation energy. These large spikes in dissipation rate are followed by a growth step in which no energy is dissipated, i.e. during the link up of the main and secondary cracks. A second, but significantly smaller spike in $R/\Gamma(x)$ is found in the Γ_{min} area. This step corresponds to the growth of the main crack through the Γ_{min} area after link up.

It is seen from Figs 4(b) and 5(b) that, at the macro-scale, a steady state condition has been reached after a crack extension of about 2.5 mm: The average values of *CTOA* and *R*, and even the local maxima and minima, remain constant during further crack extension. At the micro-scale, however, large variations appear which correspond to a sequence of local blunting and extension steps as noted in [9].

Conclusions

The paper deals with the 2D crack simulations in an elastic-plastic material which accounts for heterogeneity in the microstructure of the material. Material heterogeneity is introduced by varying the separation energy in the cohesive zone constitutive equation used to describe crack growth. The cohesive strength is kept constant.

The paper presents results for three cases of constant separation energy and for a case with spatially varying separation energy. The predicted force - load line displacement curves fall into the scatter band for experimental results. It is noted that the prediction for the case with spatially varying separation energy are close to those from the computations with a constant lower separation energy, Γ_{min} , rather oscillating about the results from the computations with the average value of separation energy, Γ_{avg}. This trend is also observed in the crack growth resistance curves based on the J-integral.

The decreased apparent toughness for the case of spatially varying separation energy can be explained by the presence of secondary cracks in front of the main crack tip. The formation the secondary cracks and their link-up with the main crack introduces strong local variations into the rate of energy dissipation. During the link-up the behaviour is that of a uniform debonding across the remaining ligament between main and secondary crack : a process occurring with significantly reduced dissipation.The present results shed light on the attempts to determine the separation energy (and thus cohesive zone parameters to be used in computational studies) from fracture surface measurements. The use of "averages" over the local variables, i.e. the average dimple height, on the fracture surface might in fact not be sufficient to characterize a material.

References

1. Stüwe, H.P., *Eng. Fract. Mech.*, vol. **13**, 231-236, 1980.
2. Stüwe, H.P., In: *Three-dimensional Constitutive Relations and Ductile Fracture*, S. Nemat-Nasser, ed., North-Holland, Amsterdam, 213-221, 1981.
3. Kolednik, O. and Stüwe, H.P., *Engineering Fracture Mechanics* **21**, 145-155, 1985.
4. Stampfl, J., Scherer, S., Gruber, M. and Kolednik, O., *Appl. Phys.*, vol. **A63**, 341-346, 1996.
5. Scherer, S. and Kolednik, O., *Microscopy and Analysis*, vol. **70,** 15-17, 2001.
6. Stampfl, J., Scherer, S., Stüwe, H.P. and Kolednik, O., In: *Mechanisms and Mechanics of Damage and Failure, Proc. of ECF 11,* J. Petit, ed., EMAS, U.K., vol. **3**, 271-276, 1996.
7. Stampfl, J. and Kolednik, O., *International Journal of Fracture* **101**, 321-345, 2000.
8. Miserez, A., Rossoll, A., Mortensen, A., *Acta Mater*, vol. **52**, 1337-1351, 2004.
9. Turner, C.C. and Kolednik, O., *Fatigue Fract. Eng. Mater. Struct.* vol. **17,** 1089-1107, 1994.
10. Yan, W.Y., Shan, G.X., Kolednik, O. and Fischer, F.D., *Key Engineering Materials* **145-149**, 179-184, 1998.
11. Chen, C.R., Kolednik, O., Scheider, I., Siegmund, T., Tatschl, A. and Fischer, F.D., *Int. J. Fracture*, vol. **120**, 517-536, 2003.
12. Shan, G.X., Kolednik, O., and Fischer, F.D., *ASTM STP* **1224**, 71-87, 1995.
13. ABAQUS (2002). Version 6.3., H.K.S. Inc., Pawtucket, U.S.A.

14. Needleman, A., *Journal of Applied Mechanics* **54**, 525-531, 1987.
15. Li, W.Z., Siegmund, T., *Eng. Fract. Mech.*, vol. **69**, 2073-2093, 2002.